Flow Dynamics and Mixing of a Transverse Jet in Crossflow—Part I: Steady Crossflow

Liwei Zhang
School of Aerospace Engineering,
Georgia Institute of Technology,
Atlanta, GA 30332
e-mail: liwei@gatech.edu

Vigor Yang[1]
William R. T. Oakes Professor and Chair
School of Aerospace Engineering,
Georgia Institute of Technology,
Atlanta, GA 30332
e-mail: vigor.yang@aerospace.gatech.edu

A large-eddy-simulation-based numerical investigation of a turbulent gaseous jet in crossflow (JICF) is presented. The present work focuses on cases with a steady crossflow and two different jet-to-crossflow velocity ratios, 2 and 4, at the same jet centerline velocity of 160 m/s. Emphasis is placed on the detailed flow evolution and scalar mixing in a compressible, turbulent environment. Various flow characteristics, including jet trajectories, jet-center streamlines, vortical structures, and intrinsic instabilities, as well as their relationships with the mixing process, are examined. Mixing efficiency is quantified by the decay rate of scalar concentration, the probability density function (PDF), and the spatial and temporal mixing deficiencies. Depending on the jet-to-crossflow velocity ratios, the wake vortices downstream of the injector orifice can either separate from or connect to the main jet plume, and this has a strong impact on mixing efficiency and vortex system development. Statistical analysis is applied to explore the underlying physics, with special attention at the jet-center and transverse planes. [DOI: 10.1115/1.4035808]

1 Introduction

Transverse jet in crossflow (JICF) is a fundamental flow configuration with a wide variety of industrial, environmental, and aerospace applications. Figure 1 shows a schematic of the JICF configuration and its characteristic flow features. Comprehensive reviews are presented in Refs. [1–4]. While significant progress has been made in this field, previous works [5–44] have mainly been concentrated in the incompressible flow regime, using water or low-speed gases as the working fluids, and gaseous jets at high subsonic speeds and moderate velocity ratios are rarely discussed. The present work aims to bridge this gap and investigates compressible, turbulent gaseous JICF by means of high-fidelity numerical simulation and state-of-the-art data analysis techniques.

Recent research pertinent to the present work—unmodulated, subsonic, single jet in crossflow—is revisited here. Tables 1 and 2 summarize the previous experimental and numerical studies, respectively. These efforts have illuminated the interactions among the jet, crossflow, and wall boundary layers and shown how the interactions generate complex vortical structures, which are commonly categorized into four groups: (1) jet shear-layer vortices in the immediate mixing region after injection; (2) horseshoe vortices wrapped around the windward side of the orifice close to the crossflow boundary layer; (3) wake vortices underneath the jet plume; and (4) the counter-rotating vortex pair (CVP) along the jet trajectory and across the entire jet plume in the far field. Fric and Roshko [5] photographed smoke streaklines in a low-speed wind tunnel and noted that wake vortices originate from the boundary layer on the wall through which the jet is issued, rather than from vortex shedding during the jet–crossflow interaction. Kelso et al. [6] identified the mean topological features of the JICF and suggested that the Helmholtz instability near the jet penetration region accounts for the formation of the shear-layer vortices. These vortices then roll up and initiate the CVP in the near field. Vorticity generated in the boundary layer of the wall from which the jet is issued also contributes to the formation of the CVP through vortex entrainment in the wake region as the jet evolves downstream into the crossflow. Other prominent experimental works include Smith and Mungal [7] and Rivero et al. [8], to cite a few.

Numerical studies of the JICF configuration have been conducted with different levels of resolution and complexity. Approaches based on the Reynolds-averaged Navier–Stokes (RANS) equations have shown serious limitations in predicting highly unsteady behaviors [27]. Direct numerical simulations (DNS) [32], on the other hand, have been restricted to low or modest Reynolds number flows, owing to their high computational cost. The large-eddy simulation (LES) technique has been relatively successful and offers the possibility of expanding our understanding over a wider range of operating conditions with reasonable accuracy [25,26]. Yuan et al. [26] performed the first three-dimensional LES calculations for JICF with a turbulent wall boundary layer and examined the CVP formation, jet fluid entrainment, turbulent flow evolution, and scalar fields. Schlüter and Schönfeld [28] simulated a mixing section of a gas turbine burner and resolved both the momentum and mixing fields. Priere et al. [45] studied a rectangular channel flow equipped with five jets and mixing devices on both the upper and lower walls. Sun and Su [46] assessed various subgrid-scale (SGS) scalar-mixing models by computing a correlation coefficient between the exact and

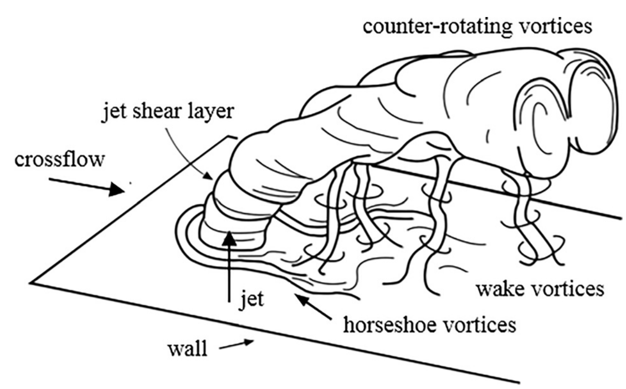

Fig. 1 Schematic of a transverse jet in crossflow and relevant flow structures [5]

[1]Corresponding author.

Contributed by the Turbomachinery Committee of ASME for publication in the Journal of Engineering for Gas Turbines and Power. Manuscript received June 14, 2016; final manuscript received December 20, 2016; published online March 21, 2017. Assoc. Editor: Riccardo Da Soghe.

Table 1 Experimental studies of subsonic, unmodulated, single jet in crossflow

			Jet conditions			
Reference	Fluid	r	Configurations	Velocity (m/s)	Re	Approach
Fric and Roshko [5]	Air	2–10	Round	1.5, 3.0, and 4.5	3.8×10^3–1.14×10^4 for CF	Smoke streaklines
Kelso and Smits [9]	Water	2–8	Round	0.047–0.182 for CF	1.2×10^3–4.6×10^3 for CF	Hydrogen bubble wire visualization
Kelso et al. [6]	Water and air	2–6	Round	1.0 CF	440–6200 CF	Flying-hot-wire
Eiff and Keffer [10]	Air	3	Elevated and round	18	3.8×10^4	PRT and hot-wire
Haven and Kurosaka [11]	Water	0.4–2.0	Round, elliptical, and rectangular	0.08 for CF	1040–2900 for CF	LIF and PIV
Smith and Mungal [7]	Air	5–25 and 200	Round	5.0 and 2.5 for CF	8.4×10^3–4.15×10^4	Hot-wire and PLIF
Han et al. [12]	Air	5, 10, and 20	Round, angled at 0 deg, ± 15 deg, ± 30 deg, and ± 45 deg	1.65 for CF	2.6×10^3, 5.2×10^3, and 10.4×10^3	Mie scattering
Hasselbrink and Mungal [13]	CH_4 jet and air CF	10 and 21	Round, nonreacting, and flame	21.3 and 45.5	6×10^3 and 1.28×10^4	PIV and PLIF
Rivero et al. [8]	Air	3.8	Circular	20	6.6×10^3 for CF	Hot-wire, PRT, and PLIF
Camussi et al. [14]	Water	1.5–4.5	Circular	0.02 for CF	100	PIV and LIF
New et al. [15]	Water	1–5	Elliptic, AR 0.3–3.0	NA	900–5100	LIF
Su and Mungal [16]	N_2 jet and air CF	5.7	Elevated and flush-wall	16.9	5000	PLIF and PIV
Gopalan et al. [17]	Water	0.5–2.5	Round	1.96 for CF	CF 1.9×10^4	PIV
Plesniak and Cusano [18]	Air	0.5, 1.0, and 1.5	Confined rectangular angled	45.7 for CF	2.04×10^5 for CF	Mie scattering and LDV
Huang and Lan [19]	Air	0.08, 0.21, 0.37, 0.69, and 1.26	Round	NA	0–10^4	Mie scattering
Shan and Dimotakis [20]	Water	10 and 32	Round	NA	1.0×10^3–2×10^4	LIF
Jovanovic et al. [21]	Water	0.35 and 0.5	Round	0.065 and 0.11	4.2×10^3 and 7.0×10^3	PIV and LCT
Cardenas et al. [22]	Air	3	Round	NA	3000 for CF	PIV and LIF
Meyer et al. [23]	Air	1.3 and 3.3	Round	1.5 for CF	2400 for CF	PIV
Galeazzo et al. [24]	Air	4	Round	37.72	1.92×10^4	PIV and LIV

Note: Re $= U_j d/\nu$, if not otherwise noted; U_j and d are the jet velocity and diameter, respectively. Re $= U_c d/\nu$, if marked by "for CF"; U_c is the crossflow velocity, and CF stands for "crossflow."

Table 2 Numerical studies of subsonic, unmodulated, single jet in crossflow

			Jet conditions			
Reference	Fluid	r	Configuration	Velocity (m/s)	Re	Approach
Jones and Wille [25]	Air	7.34	NA	NA	5815	Incompressible, LES
Yuan et al. [26]	Water	2.0 and 3.3	Round	NA	1050 and 2100 for CF	Incompressible, LES
Chochua et al. [27]	NA	34.2 and 42.2	Circular	10.67 CF	NA	SIMPLE and standard k–ε model
Schlüter and Schuönfeld [28]	Air	2, 5, and 6	Circular	NA	8.2×10^4, 1.64×10^4, and 3.18×10^4	LES
Cortelezzi and Karagozian [29]	NA	2.5, 5.4, and 10.8	Circular	NA	NA	Vortex method
Sau et al. [30]	NA	2.5 and 3.5	Square	NA	225,300	DNS
Wegner et al. [31]	Air	0.5	Round, angled at 90 deg and ± 30 deg	6.95	2.05×10^4	LES
Muppidi and Mahesh [32]	NA	1.52 and 5.7	Round	NA	1500 and 5000	Incompressible DNS
Iourokina and Lele [33]	NA	1.52	Round	NA	1500	LES
Yang and Wang [34]	Water	3, 5, and 7	Circular, inclined 45 deg	NA	5000 for CF	SIMPLE and standard k–ε model
Guo et al. [35]	NA	0.1 and 0.48	Angled at 90 deg and 30 deg	NA	4×10^5 for CF	LES
Li et al. [36]	NA	8.45, 4.97, 8.38, 4.96, 8.55, and 5.37	Circular	84.46, 114.89, and 188.09	63,165, 73,917, and 59,849	FLUENT, standard k–ε, and RNG models
Majander and Siikonen [37]	Air	2.3	Round	NA	4.67×10^4	Incompressible SIMPLE and LES
Pathak et al. [38]	Water	6	Heated, rectangular	0.3	1500	FLUENT SIMPLE standard k–ε and RSTM
Reddy and Zaman [39]	Air	6	Round, no-tab, and tabbed	NA	NA	RANS one-equation model
Salewski et al. [40]	Water	4	Circular, elliptic, and square	0.1 for CF	1×10^4 for CF	Incompressible, LES
Jouhaud et al. [41]	Air	0.77	Square	53.1	9.39×10^4	LES
Morris et al. [42]	Air	3.2	Double-sided	32.67	NA	Standard and RNG k–ε, SST
Pathak et al. [38]	Water	6 and 9	Rectangular	NA	NA	Standard k–ε
Rusch et al. [43]	Air	2.33	Circular	2.71	3.74×10^4 for CF	Steady: k–ε, k–ω, SST, and BSL RSM; transient: the SST, DES, and SAS
Ziefle and Kleiser [44]	Water	3.3	Round	NA	6930	LES

Note: $\mathrm{Re} = U_j d/\nu$, if not otherwise noted; U_j and d are the jet velocity and diameter, respectively. $\mathrm{Re} = U_c d_j/\nu$, if marked by "for CF"; U_c is the crossflow velocity, and CF stands for "crossflow."

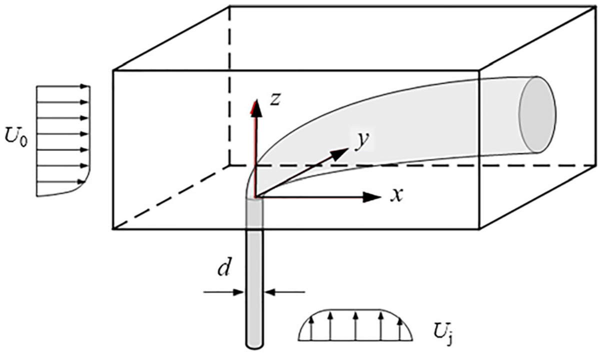

Fig. 2 Schematic of the computational domain

Table 3 Numerical grid matrices

	Grid number (million)	Average mesh size (mm)	Near-wall resolution
Grid *A*	2.8	0.15	$y^+ \approx 3$
Grid *B*	8.9	0.09	$y^+ \approx 3$
Grid *C*	29.7	0.06	$y^+ \approx 3$

modeled terms. Only slight differences were observed among different SGS models.

In addition to vortex dynamics, the mixing between the jet and crossflow fluids is a major topic of interest. This is in particular motivated by applications to gas turbine fuel injection, where fuel–air mixing is of considerable importance. For instance, in a lean-premixed gas turbine combustor, a small variation in the fuel–air equivalence ratio can lead to unexpectedly hazardous outcomes [47]. Given the significance of mixing in applications of the JICF configurations, the jet trajectory and scalar-mixing process have been examined in this study. Based on the interrelations of the jet centerline scalar concentration, jet plume penetration and spread, and turbulence levels, several scaling schemes have been proposed [7,13,16]: (1) self-similarity; (2) three length scales: r, rd, and r^2d; and (3) jetlike scaling in the near field and wakelike scaling in the far field.

The literature discussed here relates primarily to conventional cases with water or low-speed gases as the working fluid. As the speeds of concern increase to the high subsonic regime, the observations above become questionable. For example, vortex shapes are ambiguous in compressible flows and are distorted in turbulent environments, as compared with the well-defined structures in the conventional cases. Further understanding of the energy distribution and transfer among vortical structures, the dependence and influence of jet dispersion on turbulence in the flowfield, and the quantifications of mixing is also needed and is addressed in the present work. The rest of the paper is organized as follows: Section 2 describes the governing equations, computational setup, and model validation. Sections 3 and 4 discuss the results on the flow and scalar fields, respectively. Summary and conclusions are presented in Sec. 5.

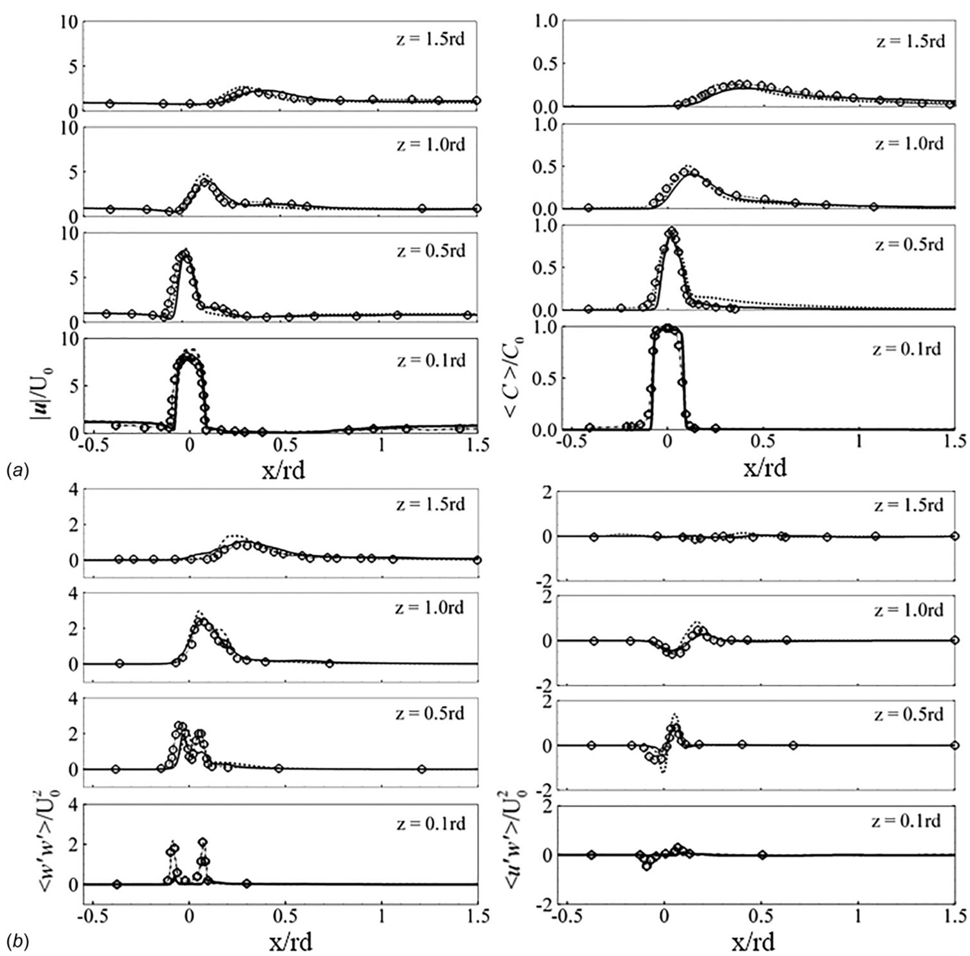

Fig. 3 Profiles of (*a*) time-averaged velocity magnitude and scalar concentration and (*b*) components of the Reynolds stress tensor in the jet-center plane (solid lines: dynamic SGS model; dashed lines: static SGS model; and symbols: experiments)

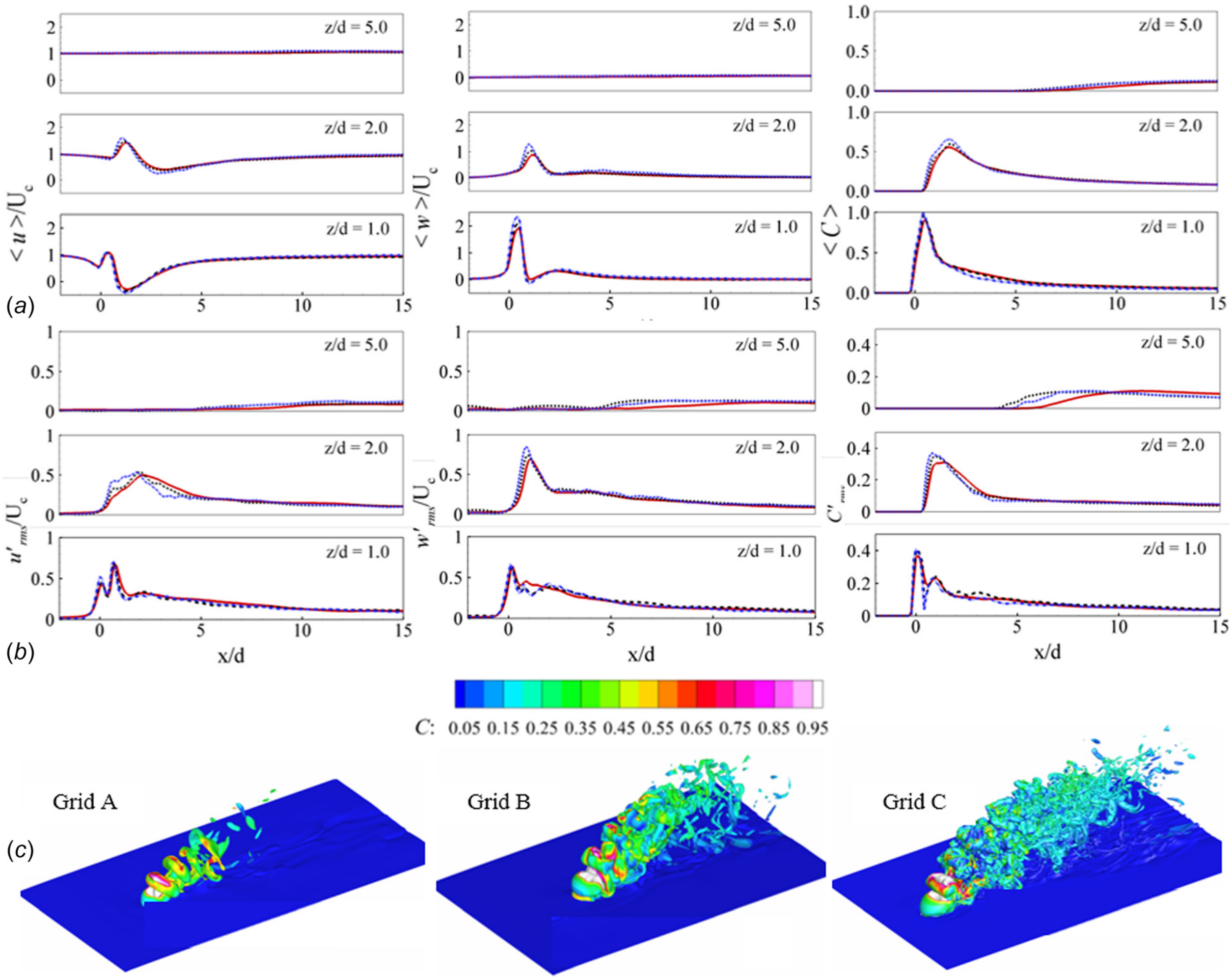

Fig. 4 Profiles of (*a*) time-averaged and (*b*) RMS of streamwise velocity, transverse velocity, and scalar concentration in the jet-center plane (red solid: grid *A*; black-dashed: grid *B*; and blue dashed–dotted–dotted: grid *C*) and (*c*) isosurfaces of vorticity magnitude $|\Omega| = 2.5 \times 10^5$/s on three grids at $t = 0.8$ ms colored by scalar concentration ($r = 2$)

2 Theoretical and Computational Framework

2.1 Governing Equations and Numerical Method. The theoretical formulation involves the unsteady, three-dimensional conservation equations of mass, momentum, energy, and species. A density-based (compressible), finite-volume methodology is used to solve the governing equations using an in-house code. Spatial discretization of the convective terms is obtained by a second-order central difference scheme, along with fourth-order artificial dissipation in generalized coordinates [48]. A fourth-order Runge–Kutta scheme is used to treat temporal integration. Turbulence closure is achieved through LES using the Smagorinsky model. Both the static and dynamic models are tested in the context of the JICF as part of the present work (described in Sec. 2.3). The static model, which has displayed great potential in several other complex cases [49,50], was chosen for the present investigation. The theoretical and numerical framework is presented in greater detail in Ref. [51].

2.2 Computational Framework. Figure 2 shows a schematic of the computational domain. The round jet orifice has a diameter (d) of 1.27 mm and is centered at the origin of the domain. The computational domain for the crossflow extends to $-5 \leq x/d \leq 16$, $-5 \leq y/d \leq 5$, and $0 \leq z/d \leq 11$ in the streamwise, spanwise, and transverse directions, respectively. The length of the jet pipe is set to be $20d$, to ensure that the pipe flow is fully developed before the jet exits the flush-wall orifice into the crossflow. To maintain realistic operating conditions, the solution in the pipe is updated at each time step, providing instantaneous flow information to the jet–crossflow interaction region. The time steps in all the calculations are fixed at 2.0×10^{-8} s for the purpose of time-accurate data extraction. The local Courant–Friedrichs–Lewy (CFL) numbers vary in the range of 0.2–0.9, depending on local flow velocities and grid sizes.

Air at ambient conditions, 1 atm and 300 K, is selected as the working fluid for both the jet and the crossflow. In order to investigate the mixing process, the jet and crossflow fluids are identified as different species, and their corresponding species conservation equations are solved separately. The mass fraction of the jet fluid is chosen as the scalar under investigation. Under realistic gas turbine conditions, the velocities of the gaseous jet and crossflow are higher than those in the experiments listed in Table 1. In their numerical work, Prière et al. [45] used 195 m/s for the jet and 60 m/s for the crossflow, in an attempt to assess the performance of mixing devices in a combustor chamber. In the present work, the crossflow velocities, U_c, for cases at jet-to-crossflow velocity ratios, r, of 2 and 4 are set to be 80 and 40 m/s, respectively. At the jet pipe entrance, a mean velocity profile from the turbulent channel flow results in Eggels et al. [52] is imposed, with a centerline velocity, U_j, of 160 m/s. Broadband noise with a Gaussian distribution is added to this profile with an intensity of 1% of the mean quantity, to initiate inflow turbulence [50]. The boundary layer thicknesses, $\delta_{0.95}$, are $0.1d$ at $x/d = -2.0$ in the crossflow and $0.25d$ at $z/d = -2.0$ in the jet pipe. The Reynolds number, Re_d, is 1.3×10^4, based on U_j and d. The spectrum of turbulent kinetic energy recorded at $z/d = -2.0$ in the jet pipe follows the Kolmogorov–Obukhov spectrum and confirms a fully developed turbulent flowfield in the jet pipe [51]. The turbulent Prandtl and Schmidt numbers are set to be 0.7 and 0.9, respectively.

Boundary conditions are specified according to the method of characteristics. At the jet and crossflow inlets, temperatures and velocities are fixed at the aforementioned values, and pressures are extrapolated from interior points. At the outlet and the top of the crossflow domain, flow properties are extrapolated from interior points, except for pressures, which are fixed at 1 atm. A buffer region is introduced downstream of the computational domain to avoid artificial wave reflections. Adiabatic and no-slip conditions are enforced at the surface of the jet pipe and the bottom wall of the crossflow domain. At the spanwise boundaries, flow symmetry is enforced to mimic an unconfined environment.

Grid resolution was chosen to fully utilize the LES technique within the computational constraints. At $Re_d = 1.3 \times 10^4$, the Kolmogorov and Taylor microscales are

$$\eta \approx d \cdot Re_d^{-3/4} = 0.001\,\mathrm{mm} \tag{1}$$

$$\lambda \approx d \cdot Re_d^{-1/2} = 0.011\,\mathrm{mm} \tag{2}$$

Table 3 summarizes the three different grid levels considered, with a refinement ratio of 1.5 in each direction. The average mesh sizes of all the three grids are comparable with the Taylor microscale and satisfy the grid requirements for the LES calculations. For all the three grids, the grid points are clustered in regions with stiff flow gradients, and the near-wall resolution is $y^+ = 3$ to adequately treat boundary layers.

2.3 Model Validation. The overall approach has been validated against a variety of vortical flow problems to establish its credibility [49–51]. Both static and dynamic SGS models are further examined here by simulating the test case of Su and Mungal [16]. Their experiments were conducted in an updraft wind tunnel, with a round jet pipe of inner diameter 4.53 mm, average jet

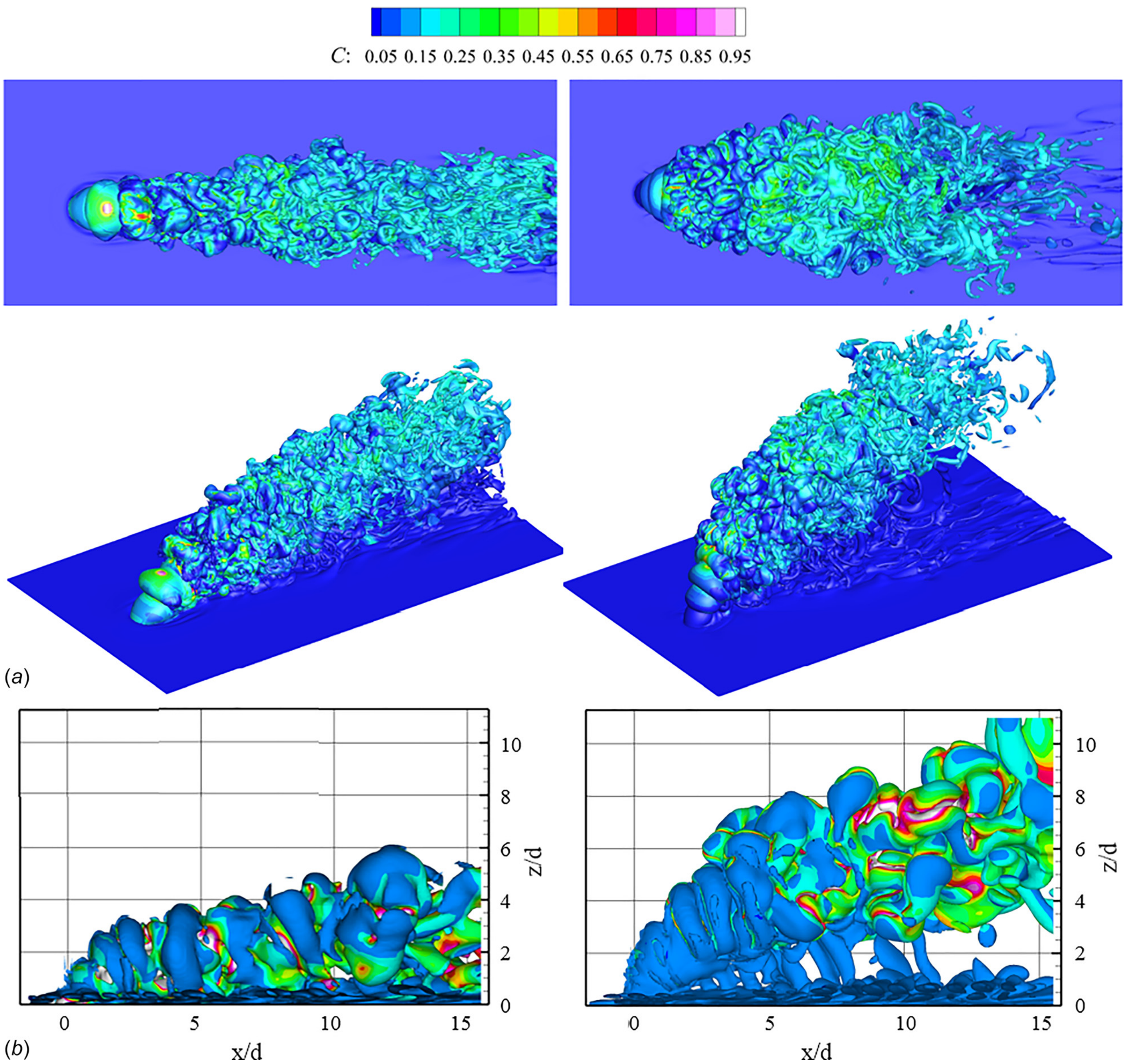

Fig. 5 Instantaneous flowfield for $r = 2$ (left) and 4 (right) at $t = 0.8$ ms: (*a*) isosurface of vorticity magnitude $|\Omega| = 1.25 \times 10^5$/s and (*b*) isosurface of helicity $H = 2.5 \times 10^5\,\mathrm{m/s^2}$. Colored by scalar concentration.

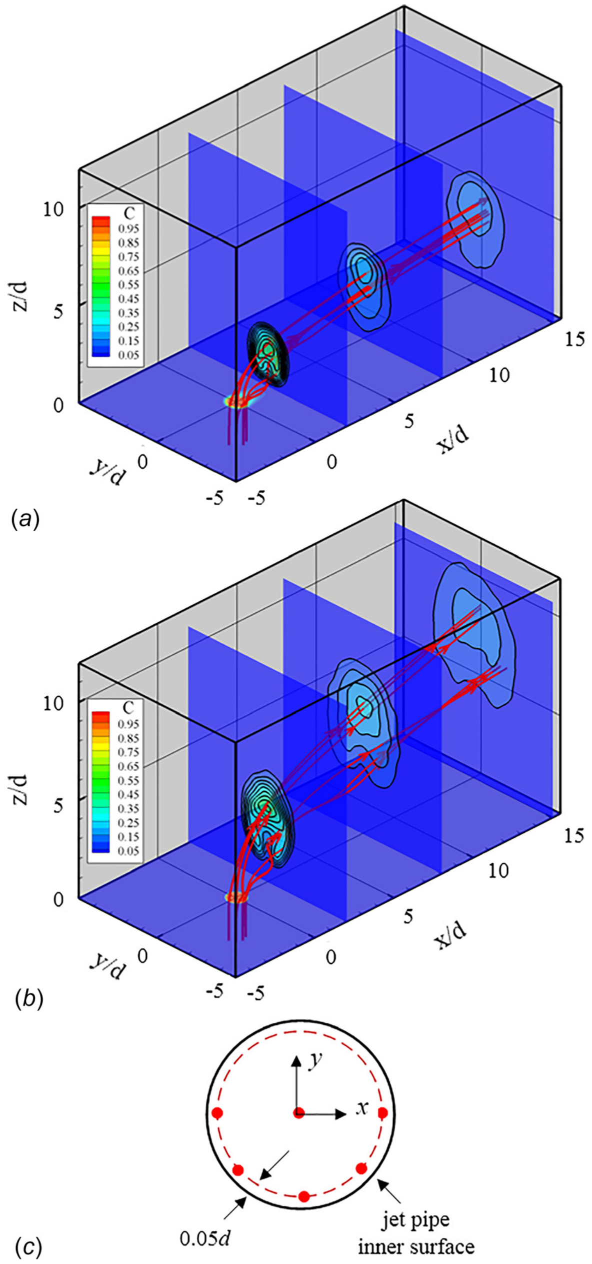

Fig. 6 Three-dimensional streamlines of the time-averaged flowfield: (*a*) $r = 2$, (*b*) $r = 4$, and (*c*) streamline traces in the $z/d = -2$ plane

velocity of 16.9 m/s, and crossflow velocity of 2.95 m/s, corresponding to

$$r = U_j/U_c = 5.7 \tag{3}$$

Figure 3 compares the computed profiles of the time-averaged velocity magnitude, scalar concentration, and stress terms in the jet-center plane, the $y = 0$ plane, with experimental measurements. The rd scaling is used here for consistency with the original presentation of the data in Ref. [16]. Just above the exit of the jet injector orifice, at $z = 0.1rd$, the profile of mean velocity magnitude is similar to that of a turbulent pipe flow, except for a trough upstream of the orifice. This is because the jet acts as an obstacle to the crossflow, thereby increasing the pressure and reducing the speed in its immediately upstream. The profile of the time-averaged scalar concentration resembles that of a free jet and is symmetrical with respect to the location of its peak value. Starting at $z = 0.5rd$, where the jet is still almost transverse to the crossflow, the profiles of both the velocity magnitude and the scalar concentration increase on the leeward side, an indication of the entrainment of jet fluid into the wake region. Figure 3(*b*) shows two components of the Reynolds stress tensor nondimensionalized with respect to the crossflow velocity. Close to the jet exit, the simulation results, especially the ones with the dynamic SGS model, are smaller than those in the experiment, suggesting the need for closer attention to the immediate vicinity of the jet orifice. At the other three locations, simulations based on both the dynamic and the constant coefficient models agree well with the experimental data. To avoid incurring the additional computational burden of the dynamic SGS model, the constant coefficient SGS model is used in the rest of the study.

3 Flow Dynamics

3.1 Vortex System and Crossflow Entrainment. The effect of grid resolution is assessed by comparing profiles of velocity and scalar concentration, as well as vortical structures, among the three grid sets. Figures 4(*a*) and 4(*b*) show the profiles of the time-averaged and root-mean-square (RMS) velocities and scalar concentrations in the jet-center plane for the case $r = 2$. At $z/d = 1.0$, a trough is observed on the windward side of the jet for $\langle u \rangle / U_c$, and no jet fluid is detected; $\langle C \rangle$ remains at a value of zero there, indicating the blockage effect of the transverse jet on the crossflow. On the lee side of the jet, $\langle u \rangle / U_c$ recovers to unity at $z/d = 1.0$ and further exceeds unity at $z/d = 2.0$ as the transverse motion $\langle w \rangle / U_c$ decreases. The $\langle w \rangle / U_c$ profile at $z/d = 1.0$ is nearly symmetric around the position of peak velocity, except for a trough in the tail on the lee side, which is also observed in the $\langle u \rangle / U_c$ profile, representing a local recirculation flow. The $\langle C \rangle$ profile departs noticeably from the corresponding velocity profiles by showing a broad elevated tail on the positive-x side, indicating that jet fluid has been advected into the wake region on the lee side of the jet. The variation of velocity profiles and the rapid decrease of scalar concentration occur in the near-field region $-2.0 < x/d < 5.0$, which encompasses the most dynamic processes in the jet/crossflow interactions. As indicated by the RMS profiles, the velocities and scalar tend to be more synchronized and the variations are only observed around the shear-layer locations in the early jet plume. Figure 4(*c*) shows the isosurfaces of vorticity magnitude at a value of 2.5×10^5/s at the same instant after jet injection. Finer grids capture more detail of the small-scale structures, but the dominant large-scale near-field coherent structures appear in all the three grids. In the far field, the flowfield becomes chaotic and the mixing relies more on the small-scale motion. The intermediate grid level B was selected for the computations described in the rest of Sec. 3 and in Sec. 4 (except for the discussions of jet trajectories and spatial evolution of mixing indices, illustrated in Figs. 9 and 14), in order to ensure reasonable predictions at an affordable level of computational expense.

Figure 5(*a*) shows the isosurfaces of the instantaneous vorticity magnitude for $r = 2$ and 4. The focus value is 1.25×10^5/s, which is equivalent to U_j/d. The vorticity in the wall boundary layer is concealed by brightness modulation to highlight the mixing region. Close to the jet exit, spanwise rollers appear in sequence on the windward side of the jet plume, demonstrating the shear-layer vortices in the initial jet region induced by the Kelvin–Helmholtz instability. As the jet enters the crossflow, the shear layer becomes unstable and rolls up into small vortices. These dynamic structures are then advected downstream and further enhanced by the entraining crossflow, forming the wavy upper boundary of the jet plume. On the leeward jet periphery, the shear layer encounters a weaker adverse pressure gradient and less crossflow entrainment, consequently yielding fewer roll-up vortices. On the lateral sides of the jet, the well-organized vortex ring is not obvious, because of the azimuthal variation of the nature of the Kelvin–Helmholtz instability around the circumference of the jet. As the crossflow deflects around the jet, it accelerates on the lateral sides and induces a skewed mixing layer. Hanging vortices are thus produced in the direction of the mean convective velocity, $\mathbf{U}_{\mathrm{mean}} = \mathbf{U}_{\mathrm{c}} + \mathbf{U}_{\mathrm{j}}$ [26]. The jet fluid carried by the hanging vortex gains horizontal momentum and merges into the lower half of the jet plume, as shown in Fig. 6. Both the spanwise rollers and the hanging vortices lose regularity and gradually break down as the jet moves downstream, and the flowfield becomes highly turbulent. The CVP is embedded in the fine scale turbulent structures. (The CVP will be discussed later with reference to the time-averaged flowfield.) Although the cases with $r = 2$ and 4 have similar appearances, the latter shows a broader plume and more fine scale turbulence in the far field, an indication of more intensified transport along the jet trajectory.

The fingerlike, roller-structured wake vortices play an important role in crossflow entrainment and vorticity transport from the near-wall region to the jet plume. Wake vortices have their origins, as proposed by Fric and Roshko [5], in the crossflow boundary layer that develops upstream of the jet injection orifice. As the crossflow sweeps around the transverse jet, it encounters an adverse pressure gradient on the jet leeside, inducing the first boundary layer separation in the early wake region. Tornadolike vortices emanate from the separation zone and reach up toward the jet plume (see Fig. 1). As these vortices convect downstream, new vorticity is generated at the wall and fed into the wake structures. They are found beneath the jet plume and are shown by isosurfaces of helicity at $2.5 \times 10^5\,\mathrm{m/s^2}$ in Fig. 5(*b*). Since helicity reflects values of speed and vorticity and the relative angle between them, high helicity is indicative of the core region of a vortex. In both cases, the crossflow boundary layer serves as a source that produces and transfers vorticity toward the jet plume. While for case $r = 2$, the jet plume stays close to the wall and interacts with the crossflow boundary layer, for $r = 4$ the helicity isosurfaces penetrate deep into the jet region, and the tornadolike wake structures are well-formed in the downstream region. The absence of jet fluid in these vertical rollers suggests strong entrainment of the crossflow fluid into the jet plume.

Horseshoe vortices are generated by the separation of the crossflow boundary layer on the windward and lateral sides of the jet. As the crossflow approaches the jet, it encounters a streamwise adverse pressure gradient ahead of the jet, which induces flow deceleration, separation, and recirculation, thereby creating the early horseshoe vortices. These vortices are weak in compressible flows and are shown by the two-dimensional streamlines in Fig. 7. Kelso and Smits [9] found that horseshoe vortices could be steady, oscillating, or coalescing, depending on the flow conditions. Due to similarity in their formation mechanisms, there may be a connection between the horseshoe and wake vortices.

Figure 8 shows the snapshots of scalar concentration in the jet-center plane. For $r = 2$, counterclockwise-rotating vortices are formed on the windward jet periphery. They are backward-rolling vortices and typically occur in cases with relatively low velocity ratios [19]. The gaps between adjacent vortices provide favorable regions for the crossflow to be entrained by the jet fluid. The length of the jet potential core is around $2.0d$, the gaps between the rolling vortices are about $1.5d$, and the vortices disappear at $x/d \approx 4.0$. The jet plume has a thick brush in the wake region and shows a high tendency to reach the tunnel wall. For $r = 4$, the shear-layer vortices closely resemble jetlike vortices, appear intermittently on the windward side of the jet plume, and disappear without periodicity [19]. Gaps between vortices decrease to below $1.0d$. The rare shear-layer vortices on the leeward side of the jet have little regularity. The jet potential core extends to $x/d = 2.5$, after which the shear-layer vortices disappear and the jet fluid loses continuity and breaks down into the crossflow. Intense motion occurs in the region of $0.5 < x/d < 3.0$ and $2.5 < z/d < 5.0$, where pockets of jet fluid first roll up, then elongate, and

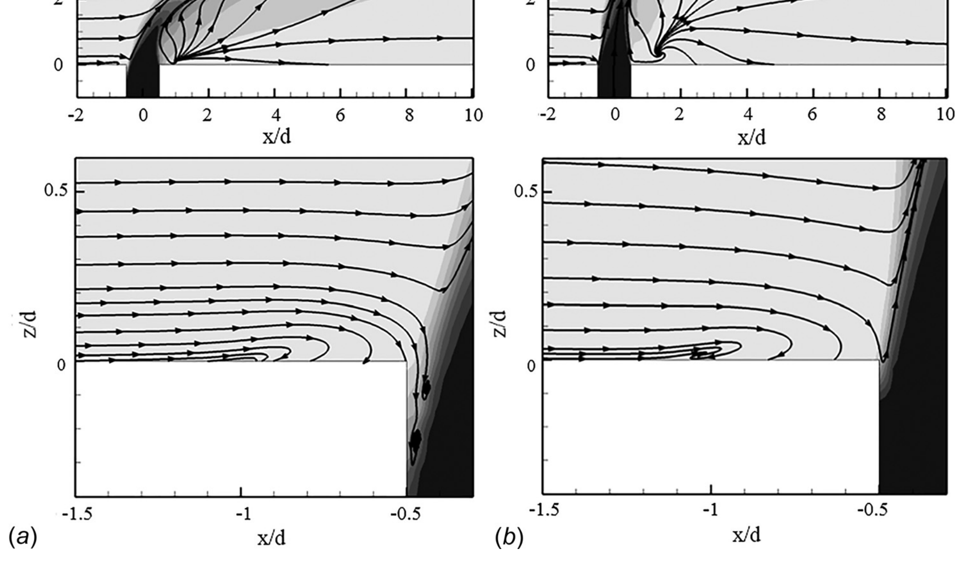

Fig. 7 Two-dimensional streamlines of the time-averaged flowfield in the jet-center plane: (*a*) $r = 2$ and (*b*) $r = 4$. Scalar concentration is shown in grayscale.

eventually detach from the jet potential core. This area is recognized as the end of the near field. Further downstream, even though zones with a relatively high concentration of jet fluid still exist, the jet fluid is more dispersed into the crossflow and mixing takes place extensively but at a modest intensity. For $r = 2$, spatially periodical vortical structures are observed in the near field, and chaotic dispersion of small rollers prevails in the far field. For $r = 4$, similar observations apply, although the turbulent rollers appear to be much smaller and closer in a higher jet plume.

3.2 Jet Trajectory and CVP Development. There are some discrepancies in the definition of jet trajectory in the literature. In the present work, the time-averaged streamline across the center of the jet exit—the jet-center streamline—is recorded to represent the jet trajectory. Figure 9 shows the traces of the jet trajectory and the jet plume boundaries marked by a scalar concentration of 0.05 on the jet-center plane. The overlap of the trajectories from the three different grids suggests reasonable grid convergence. Since the leeward side of the jet encounters less crossflow entrainment and mixing, the lower plume boundary starts further down in the wake region, rather than immediately at the orifice. For both the $r = 2$ and 4 cases, plume boundaries are asymmetric with respect to the jet trajectory. The lower boundary of the $r = 2$ jet almost touches the tunnel wall, while the jet penetrates deeper into the crossflow in the $r = 4$ case.

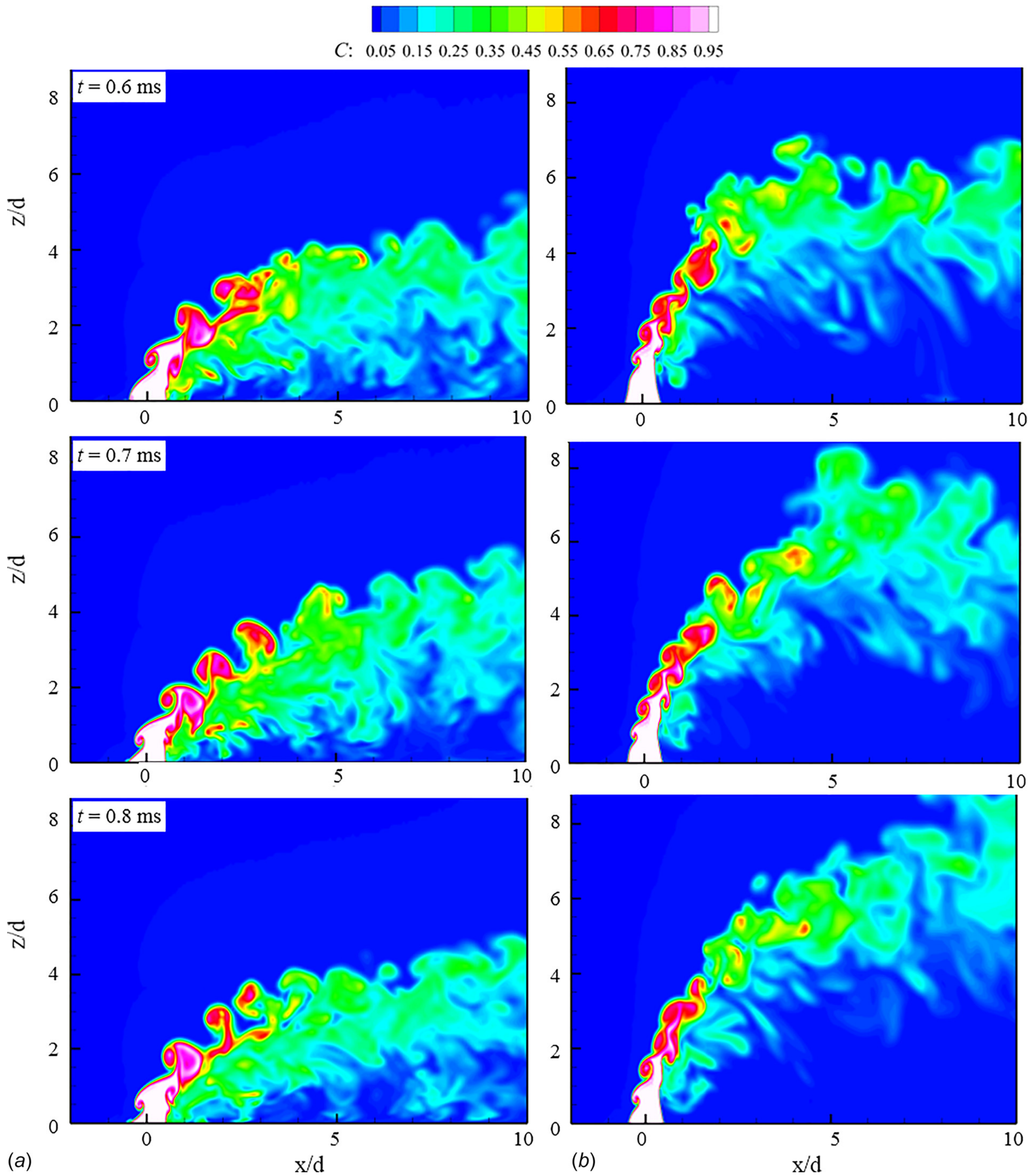

Fig. 8 Temporal evolution of scalar concentration in the jet-center plane: (*a*) $r = 2$ and (*b*) $r = 4$

Figure 7 shows the two-dimensional streamlines in the jet-center plane colored by the scalar concentration. The incoming crossflow streamlines curve up ahead of the orifice, and a few also enter the jet pipe and form hovering vortices in the $r = 2$ case. Closeup views show a decreased scalar concentration inside the pipe as a result of this crossflow entrainment. A weak horseshoe vortex appears immediately upstream of the orifice in the $r = 4$ case. A stagnation point is found in the downstream region at around $x/d = 1.0$ with a positive divergence, suggesting crossflow boundary layer separation in the early wake region.

Jet trajectory is the result of two motions: transverse motion pushing the jet away from the wall and streamwise motion carrying it downstream with the crossflow. The CVP aligned with the trajectory demonstrates the global flowfield induced by the transverse impulse. Figures 6(*a*) and 6(*b*) show the three-dimensional streamlines in the time-averaged flowfield and contours of the time-averaged scalar concentration on three transverse planes. All of the six streamlines originate from the jet pipe and develop in the $y < 0$ zone. Figure 6(*c*) shows a schematic of the streamline traces in the $z/d = -2.0$ plane; one streamline passes through the pipe center, and the other five cross the circumferential line at a distance of $0.05d$ from the pipe wall and have an azimuthal spacing of $\pi/4$ from each other. The three streamlines on the jet-center plane follow their original trend and penetrate deeply into the crossflow as part of the main jet plume. The three streamlines on the lateral side, however, bend in the streamwise direction, twist around the plume, and converge to the tails of the kidney-shaped profiles. This observation can be explained by the downstream path of the jet fluid shaped by the hanging vortices [26]. On the lateral sides of the jet, skewed mixing layers are formed as the crossflow deflects around the jet body. Vortical structures form therein and grow in the direction of the mean convective velocity, carrying a strong axial flow [53]. These hanging vortices encounter an adverse pressure gradient as they move downstream and thus gradually break down, initializing the nascent CVP, mainly in the lower part of the jet boundary. Note that for the $r = 2$ case, the kidney shape is not observed in the scalar concentration contours, possibly because the jet plume remains close to the boundary layer flow and typical JICF structures are not well developed.

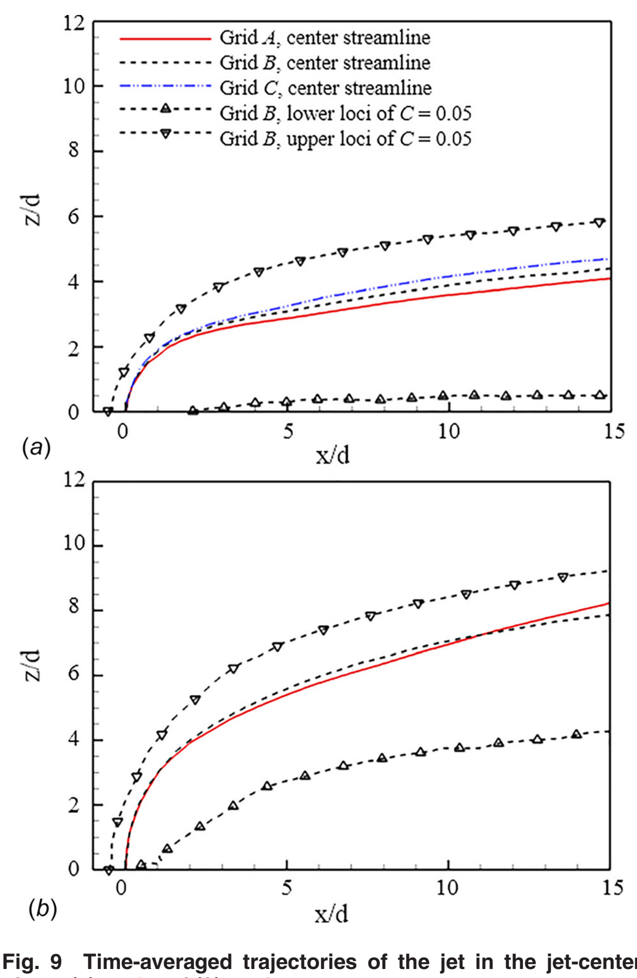

Fig. 9 Time-averaged trajectories of the jet in the jet-center plane: (*a*) $r = 2$ and (*b*) $r = 4$

Figure 10 shows the spatial evolution of the time-averaged scalar concentration with two-dimensional streamlines for the $r = 4$ case. The CVP is clearly presented by the streamline spirals centered at the tails of the kidney-shaped profiles. This is the dominant motion in the far field and accounts for most of the scalar mixing by large-scale momentum transport. As fluid in the wake region is carried into the jet plume, the spacing between the tails of the CVP increases downstream. Jet fluid in the plume drifts transversely and disperses across a broad region into the crossflow. This interaction occurs all the way downstream with diminishing intensity. A pair of secondary vortices also appears in the streamlines near the crossflow wall [54].

Figure 11 shows a sequence of slices normal to the center streamline of the time-averaged flowfield. For the purpose of brevity, only the $r = 4$ case is presented here. Starting from the coordinate origin at the center of the jet exit plane, the first slice is $0.5d$ away from the jet orifice. Both the scalar concentration and the transverse velocity contours show horseshoe-shaped potential cores. The tails of the horseshoes reveal that immediately after injection, a small portion of the jet fluid, mostly at the lateral sides, is blown downstream and twisted in the leeward side of the main jet plume. The second slice is about $2.5d$ away from the orifice, where the potential core almost disappears and the jet plume is more deformed, yielding a much larger kidney-shaped profile. In the transverse velocity contour, two peak zones are observed, approximately $2.0d$ away from each other, one in the jet plume and the other in the wake region. The latter is a secondary flow, and its location coincides with the spacing in the kidney-shaped contour of scalar concentration. It corresponds to the node (stagnation point) in the streamlines in Fig. 7, which is induced when the crossflow bypassing the jet blockage separates in the low-pressure region and is further carried away by the upward-moving jet fluid. The third slice, about $5.0d$ away from the orifice, shows the same trend. Further downstream, the plume size increases and the scalar concentration and transverse velocity decrease.

4 Scalar Mixing: Characteristics and Quantification

Mixing efficiency is strongly affected by unsteady flow characteristics, especially in the JICF configuration, due to the concurrent presence of complex vortical structures. Scalar mixing under the influence of flow unsteadiness is examined in this section, and a quantification based on statistical analysis is presented.

4.1 Decay of Scalar Concentration and Velocity. Figure 12 plots the spatial variation of the maxima (over the x-planes) of the local scalar concentration and the normalized transverse velocity on a log–log scale based on the time-averaged flowfield for the $r = 2$ and 4 cases. The two flow properties do not converge with each other, but they have the same slopes in certain regions. Near the jet exit, a classic jet potential core is observed, followed by a decrease with a slope of $\kappa \sim -0.37$ beginning at $x/d \sim 0.8$. Irregularity appears in the region $1.0 < x/d < 4.0$, corresponding to the areas where the jet fluid pockets are shed into the crossflow. Starting from $x/d \sim 5.0$, all the curves have a decreasing rate of $\kappa \sim -0.77$, exhibiting smooth mixing in the far field. A decay rate of -0.67 was reported in Ref. [7] for $r \geq 5$ cases in the downstream regions covered by the current simulations. There are at least three possible explanations of the difference between Fig. 12 and the results reported in Ref. [7]: (1) in Ref. [7], predictions were based on the downstream distance, s, rather than the axial coordinates, x, even though $s \approx x$ in the far field; (2) numerical inaccuracy in the current simulations; and/or (3) the difference in jet-to-crossflow velocity ratio, r, and crossflow and jet speeds.

4.2 Point Probability Density Functions. The flowfield is probed at the following locations and the evolutions of the pressure and scalar concentration are recorded to identify intrinsic flow instabilities.

probe 07: (0.54d, 0, 2.04d)
probe 20: (4.93d, 0, 4.95d)
probe 34: (12.03d, 0, 6.67d)

These probes are located in the jet potential core, the near field, and the far field of the jet plume, respectively. All the data are recorded every 2.0×10^{-5} ms after the initial jet transience is completed and the flowfield has reached a statistically steady state. The recording periods for the $r = 2$ and 4 cases are 0.6 and 1.2 ms, respectively, equivalent to 38 U_c/d and covering more than two flow-through times.

The point probability density function (PDF) is calculated to examine the mixing characteristics at a specific location. The PDF at point x is defined as

$$f(\xi, x_i) = \{\text{probability that the event } \alpha_{ik} = \xi \text{ occurs}\} \qquad (4)$$

where ξ is the statistical representation of α (the quantity whose PDF is calculated), x_i is the specific point under investigation, i represents the spatial index of the point, and k is the index in a time series. The function $f(\xi, x_i)$ is constructed from time series α_{ik} so that the averaged quantities are obtained by integration

$$\langle \alpha_i \rangle = \int_{-\infty}^{+\infty} \xi f(\xi; x_i) d\xi \qquad (5)$$

Figure 13 shows the PDF of the scalar concentration at the probes noted above for both cases. Since probe 07 is located in the jet potential core, its PDF rises significantly near scalar concentration $C = 1$. The PDFs of the other two probes disperse around their average value and show temporal heterogeneity at their respective locations. At probe 20, which is located at $x/d \sim 5.0$ downstream of the jet exit, the $r = 4$ case shows a flatter profile, exhibiting greater inhomogeneity due to the breakup and unsteadiness of the jet plume in this region, whereas for probe 34, located at $x/d \sim 12.0$, the PDF profile shows a more concentrated distribution, demonstrating more homogeneous mixing in the far field.

4.3 Spatial and Temporal Mixing Deficiencies. Two mixing indices, the spatial mixing deficiency (SMD) and the temporal mixing deficiency (TMD) [45,54], are investigated at downstream locations $x/d = 0$, 1, 2, 5, 8, 10, 12, and 15. SMD is a measure of the spatial heterogeneity of the time-averaged flow quantity,

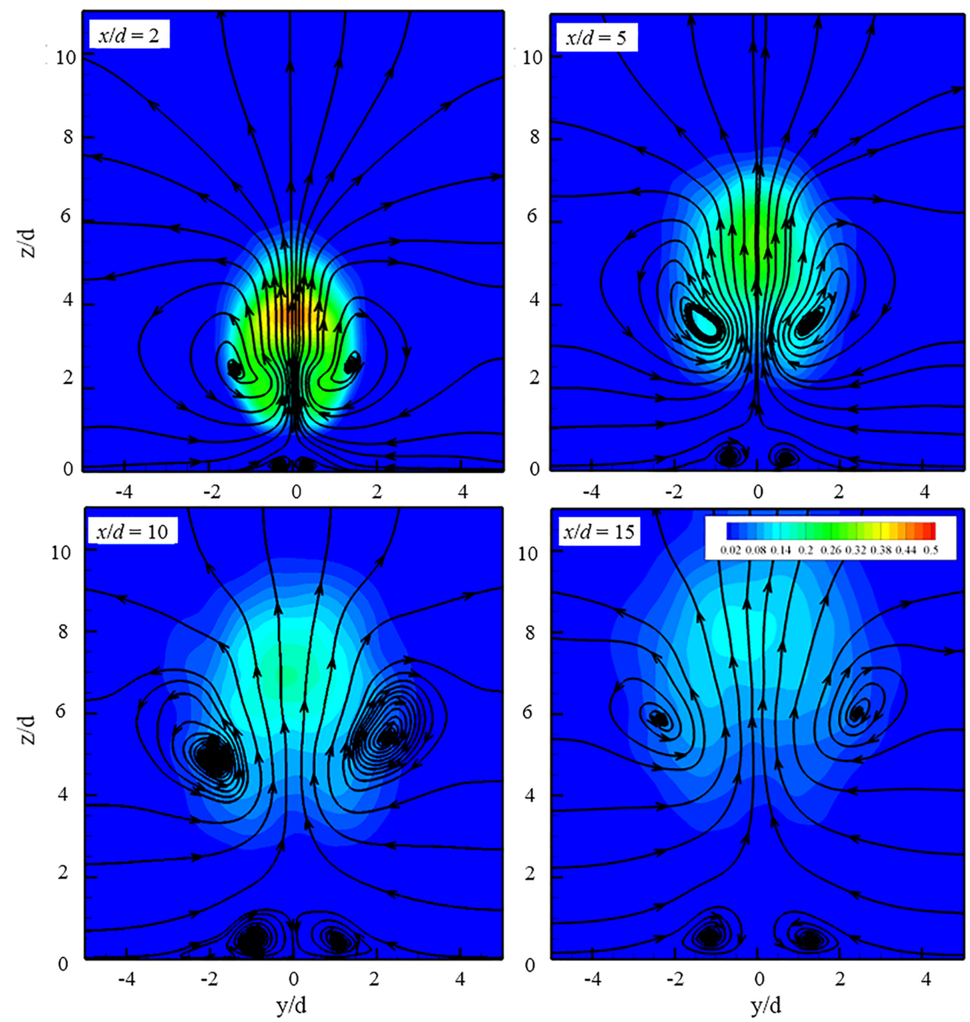

Fig. 10 Spatial evolution of the time-averaged scalar concentration with two-dimensional streamlines ($r = 4$)

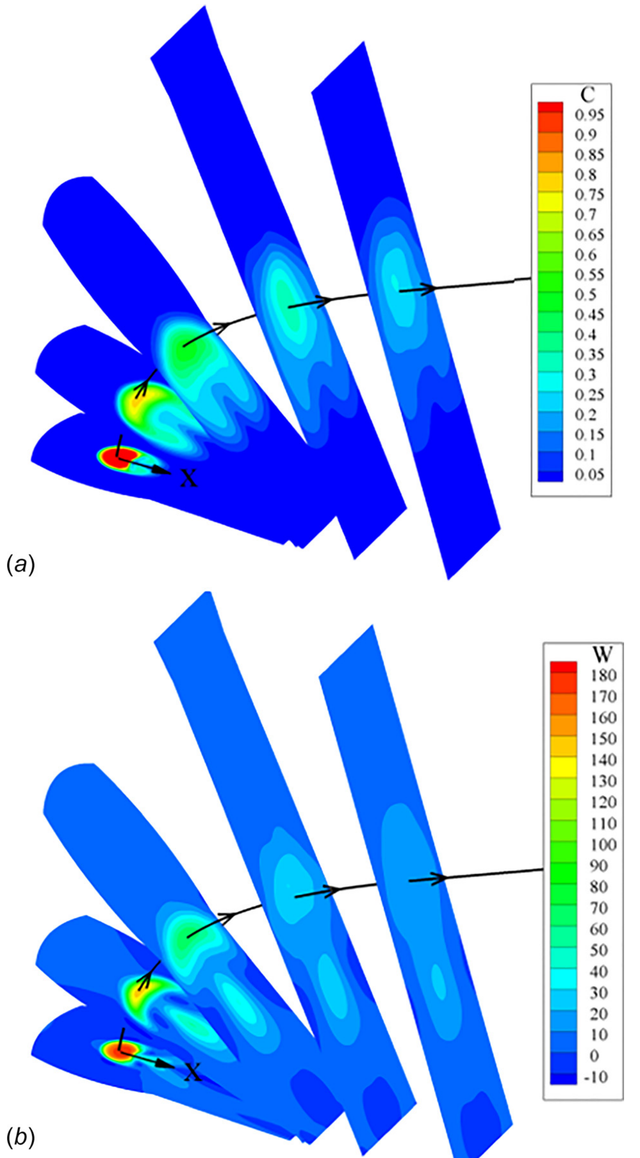

Fig. 11 Spatial evolution of the time-averaged (*a*) scalar concentration and (*b*) transverse velocity along the center streamlines ($r = 4$)

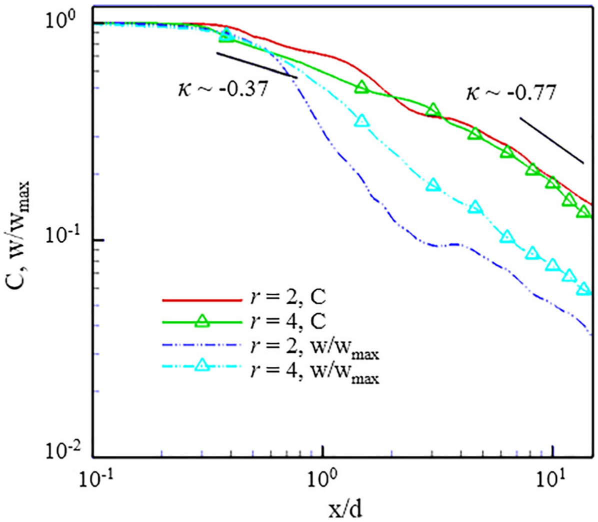

Fig. 12 Spatial evolution of the maxima (over the *x*-planes) of the local scalar concentration and the normalized transverse velocity

whereas TMD is a spatial average of the temporal heterogeneity at various points over a plane. Both indices are calculated based on the instantaneous scalar concentration over the planes of interest. Over n snapshots, SMD and TMD at point i are calculated as

$$\mathrm{SMD} = \frac{RMS_{\mathrm{plane}}(\langle C_i \rangle)}{\mathrm{Avg}_{\mathrm{plane}}(\langle C \rangle)} \tag{6}$$

$$\mathrm{TMD} = \mathrm{Avg}_{\mathrm{plane}}\left(\frac{\mathrm{RMS}_i}{\langle C_i \rangle}\right) \tag{7}$$

where

$$\langle C_i \rangle = \frac{1}{n}\sum_{k=1}^{n} C_{i,k} \tag{8}$$

$$\mathrm{RMS}_i = \sqrt{\frac{1}{n-1}\sum_{k=1}^{n}\left(\langle C_i \rangle - C_{i,k}\right)^2} \tag{9}$$

$$\mathrm{Avg}_{\mathrm{plane}}(\langle C \rangle) = \frac{1}{m}\sum_{i=1}^{m}\langle C_i \rangle \tag{10}$$

$$\mathrm{RMS}_{\mathrm{plane}}(\langle C_i \rangle) = \sqrt{\frac{1}{m-1}\sum_{i=1}^{m}\left(\langle C_i \rangle - \mathrm{Avg}_{\mathrm{plane}}(\langle C_i \rangle)\right)^2} \tag{11}$$

For the $r = 2$ and 4 cases, the calculations are performed in the regions of $-3 \le y/d \le 3$, $0 \le z/d \le 6$, and $-4 \le y/d \le 4$, $0 \le z/d \le 10$, respectively. Figure 14 shows the spatial evolution of the two indices. For the same velocity ratio, no significant difference is observed between the grids A and B, again indicating reasonable grid convergence. The complex nature of the flow produces high spatial heterogeneity in both cases, as seen from the large values of SMD, which decrease slightly downstream. There is an increasing trend in TMD in the near-field region, where highly oscillatory and unsteady behaviors are observed due to jet plume breakup, and a decreasing trend in locations $x/d > 5.0$. The values of the two indices are smaller in the $r = 4$ case than in the $r = 2$ case at all the locations, indicating that the mixing field is more homogeneous for the larger jet-to-crossflow velocity ratio.

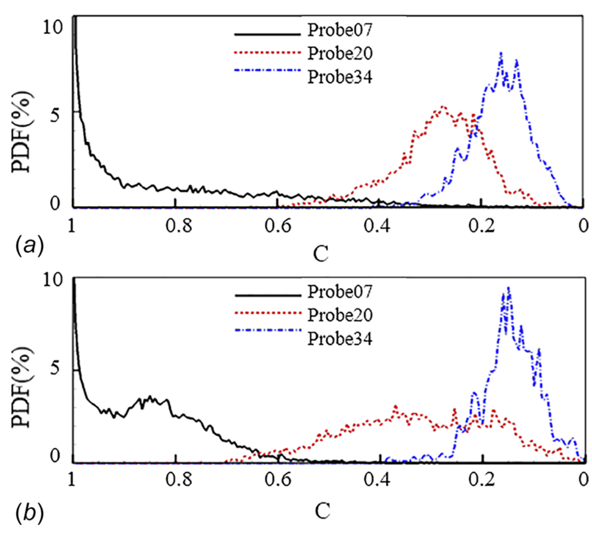

Fig. 13 Point PDF of scalar concentration at three probes: (*a*) $r = 2$ and (*b*) $r = 4$

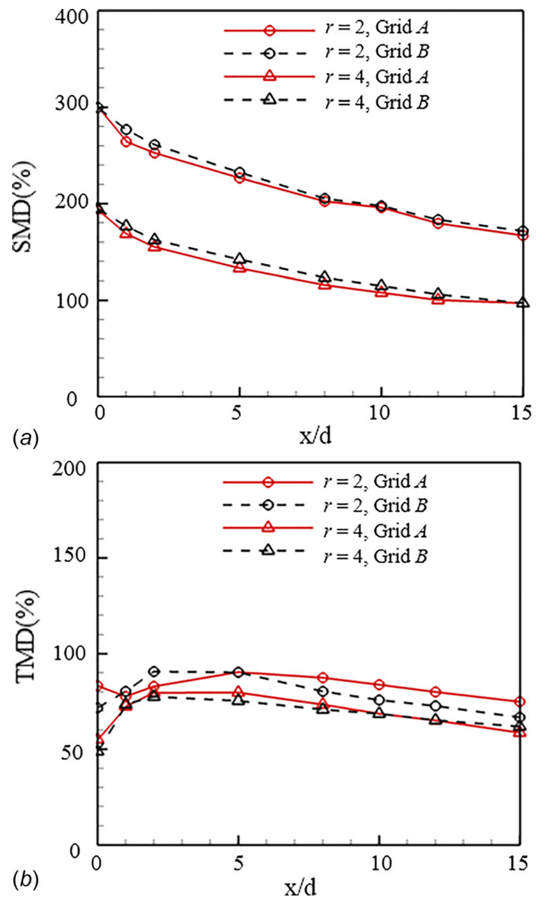

Fig. 14 Spatial evolution of mixing indices: (*a*) SMD and (*b*) TMD

5 Summary and Conclusions

This work considers flow characteristics and scalar mixing in the context of a compressible, turbulent, gaseous jet in a steady crossflow. Two different jet-to-crossflow velocity ratios, 2 and 4, are considered, and results from the two cases are presented side-by-side for comparison.

Both the instantaneous and time-averaged flowfields are analyzed. Vortex systems are identified through vorticity and helicity isosurfaces and important observations are made: (1) horseshoe vortices are detected ahead of the jet orifice, but their strength is small compared to the other vortices; (2) jet shear-layer vortices appear on the windward and leeward sides of the jet in the near field and play an important role in defining the boundary of the jet plume; (3) wake vortices appear as tornadolike structures and provide a possible connection between the jet plume and the crossflow boundary layer; (4) early formation of the counter-rotating vortex pair is closely related to the hanging vortices produced in the skewed mixing layer; (5) the strength and structure of the vortices are affected by the velocity ratio, with a higher velocity ratio producing more apparent effects; and (6) the shapes of the aforementioned vortices, especially the horseshoe and wake vortices, are ambiguous in the current high subsonic simulations, as opposed to the well-defined structures found in conventional low-speed cases. Flow compressibility and the ensuing turbulent environments are identified as the causes of ambiguity in shapes.

Scalar mixing is examined based on contours, streamlines, and slices in both Cartesian and streamline coordinates. It is linked to flow dynamics by the following processes: (1) entrainment of the crossflow by the jet, which in particular occurs at the gaps between the rolling vortices on the surface of the jet plume; (2) transportation of the crossflow fluid into the main jet body at low jet penetrations by the upright wake vortices; and (3) turbulent scalar flux within the coherent vortical structures. The latter two processes are especially prominent in the current simulations, which have relatively small jet-to-crossflow velocity ratios and large flow speeds.

Mixing efficiency is quantified through: (1) the decay rate of the scalar concentration, which is closely related to the flow dynamics; (2) the probability density function, which provides an effective method for evaluating the local mixing characteristics; and (3) spatial and temporal mixing deficiencies, which are strongly dependent on the jet-to-crossflow velocity ratios and reveal lower heterogeneity of the flowfield at high velocity ratios. Since the mixing process is closely related to flow compressibility and turbulent properties, grid resolution and the mixing model need to be carefully calibrated for better numerical accuracy in future computations. The results of the present work are more qualitative than quantitative, although the approaches demonstrated here are recommended for general studies.

Cases with oscillating crossflows are examined in Part II of the study, in a further investigation of flow and mixing phenomena.

Acknowledgment

This work was sponsored by the National Energy Technology Laboratory, U.S. Department of Energy under Grant No. DE-FG26-07NT43069.

Nomenclature

C = scalar mass fraction
d = jet diameter, mm
f = probability
k = index in a time series
n = total number of snapshots
p = pressure, atm
r = jet-to-crossflow velocity ratio
Re = Reynolds number
s = downstream distance, mm
t = time, s
U, u, v, w = velocity components, m/s
x, y, z = spatial coordinates, mm
x_i = a specific point
α = temporal quantity
δ = boundary layer thickness, mm
η = Kolmogorov microscale, mm
κ = slope
λ = Taylor microscale, mm
ξ = value of the temporal quantity
$< >$ = time-averaged

Subscripts

c, 0 = crossflow
d = jet diameter
i = spatial index of a point
j = jet

References

[1] Margason, R. J., 1983, "Fifty Years of Jet in Cross Flow Research," AGARD Symposium on Computational and Experimental Assessment of Jets in Cross-flow, Winchester, UK, Paper No. AGARD-CP-534, pp. 1–41.
[2] Karagozian, A. R., 2010, "Transverse Jets and Their Control," Prog. Energy Combust. Sci., **36**(5), pp. 531–553.
[3] Mahesh, K., 2012, "The Interaction of Jets With Crossflow," Annu. Rev. Fluid Mech., **45**(1), pp. 379–407.
[4] Karagozian, A. R., 2014, "The Jet in Crossflow," Phys. Fluids, **26**(3), pp. 1–17.
[5] Fric, T. F., and Roshko, A., 1994, "Vortical Structure in the Wake of a Transverse Jet," J. Fluid Mech., **279**, pp. 1–47.
[6] Kelso, R. M., Lim, T. T., and Perry, A. E., 1996, "An Experimental Study of Round Jets in Cross-Flow," J. Fluid Mech., **306**, pp. 111–144.
[7] Smith, S. H., and Mungal, M. G., 1998, "Mixing, Structure and Scaling of the Jet in Crossflow," J. Fluid Mech., **357**, pp. 83–122.
[8] Rivero, A., Ferré, J. A., and Giralt, F., 2001, "Organized Motions in a Jet in Crossflow," J. Fluid Mech., **444**, pp. 117–149.
[9] Kelso, R. M., and Smits, A. J., 1995, "Horseshoe Vortex Systems Resulting From the Interaction Between a Laminar Boundary Layer and a Transverse Jet," Phys. Fluids, **7**(1), pp. 153–158.

[10] Eiff, O. S., and Keffer, J. F., 1997, "On the Structures in the Near-Wake Region of an Elevated Turbulent Jet in a Crossflow," J. Fluid Mech., **333**, pp. 161–195.
[11] Haven, B. A., and Kurosaka, M., 1997, "Kidney and Anti-Kidney Vortices in Crossflow Jets," J. Fluid Mech., **352**, pp. 27–64.
[12] Han, D., Orozco, V., and Mungal, M. G., 2000, "Gross-Entrainment Behavior of Turbulent Jets Injected Obliquely Into a Uniform Crossflow," AIAA J., **38**(9), pp. 1643–1649.
[13] Hasselbrink, E. F., and Mungal, M. G., 2001, "Transverse Jets and Jet Flames—Part 2. Velocity and OH Field Imaging," J. Fluid Mech., **443**, pp. 27–68.
[14] Camussi, R., Guj, G., and Stella, A., 2002, "Experimental Study of a Jet in a Crossflow at Very Low Reynolds Number," J. Fluid Mech., **454**, pp. 113–144.
[15] New, T. H., Lim, T. T., and Luo, S. C., 2003, "Elliptic Jets in Cross-Flow," J. Fluid Mech., **494**, pp. 119–140.
[16] Su, L. K., and Mungal, M. G., 2004, "Simultaneous Measurements of Scalar and Velocity Field Evolution in Turbulent Crossflowing Jets," J. Fluid Mech., **513**, pp. 1–45.
[17] Gopalan, S., Abraham, B. M., and Katz, J., 2004, "The Structure of a Jet in Cross Flow at Low Velocity Ratios," Phys. Fluids, **16**(6), pp. 2067–2087.
[18] Plesniak, M. W., and Cusano, D. M., 2005, "Scalar Mixing in a Confined Rectangular Jet in Crossflow," J. Fluid Mech., **524**, pp. 1–45.
[19] Huang, R. F., and Lan, J., 2005, "Characteristic Modes and Evolution Processes of Shear-Layer Vortices in an Elevated Transverse Jet," Phys. Fluids, **17**(3), pp. 1–13.
[20] Shan, J. W., and Dimotakis, P. E., 2006, "Reynolds-Number Effects and Anisotropy in Transverse-Jet Mixing," J. Fluid Mech., **566**, pp. 47–96.
[21] Jovanović, M. B., de Lange, H. C., and van Steenhoven, A. A., 2006, "Influence of Hole Imperfection on Jet Cross Flow Interaction," Int. J. Heat Fluid Flow, **27**(1), pp. 42–53.
[22] Cárdenas, C., Suntz, R., Denev, J. A., and Bockhorn, H., 2007, "Two-Dimensional Estimation of Reynolds-Fluxes and -Stresses in a Jet-in-Crossflow Arrangement by Simultaneous 2D-LIF and PIV," Appl. Phys. B Lasers Opt., **88**(4), pp. 581–591.
[23] Meyer, K. E., Pedersen, J. M., and Özcan, O., 2007, "A Turbulent Jet in Crossflow Analysed With Proper Orthogonal Decomposition," J. Fluid Mech., **583**, pp. 199–227.
[24] Galeazzo, F. C. C., Donnert, G., Habisreuther, P., Zarzalis, N., Valdes, R. J., and Krebs, W., 2011, "Measurement and Simulation of Turbulent Mixing in a Jet in Crossflow," ASME J. Eng. Gas Turbines Power, **133**(6), p. 061504.
[25] Jones, W. P., and Wille, M., 1996, "Large-Eddy Simulation of a Plane Jet in a Cross-Flow," Int. J. Heat Fluid Flow, **17**(3), pp. 296–306.
[26] Yuan, L. L., Street, R. L., and Ferziger, J. H., 1999, "Large-Eddy Simulations of a Round Jet in Crossflow," J. Fluid Mech., **379**, pp. 71–104.
[27] Chochua, G., Shyy, W., Thakur, S., Brankovic, A., Lienua, J., Porter, L., and Lischinsky, D., 2000, "A Computational and Experimental Investigation of Turbulent Jet and Crossflow Interaction," Numer. Heat Transfer Part A, **38**, pp. 557–572.
[28] Schlüter, J. U., and Schönfeld, T., 2000, "LES of Jets in Cross Flow and Its Application to a Gas Turbine Burner," Flow Turbul. Combust., **65**(2), pp. 177–203.
[29] Cortelezzi, L., and Karagozian, A. R., 2001, "On the Formation of the Counter-Rotating Vortex Pair in Transverse Jets," J. Fluid Mech., **446**, pp. 347–373.
[30] Sau, A., Sheu, T. W. H., Hwang, R. R., and Yang, W. C., 2004, "Three-Dimensional Simulation of Square Jets in Cross-Flow," Phys. Rev. E, **69**(6), p. 066302.
[31] Wegner, B., Huai, Y., and Sadiki, A., 2004, "Comparative Study of Turbulent Mixing in Jet in Cross-Flow Configurations Using LES," Int. J. Heat Fluid Flow, **25**(5), pp. 767–775.
[32] Muppidi, S., and Mahesh, K., 2005, "Study of Trajectories of Jets in Crossflow Using Direct Numerical Simulations," J. Fluid Mech., **530**, pp. 81–100.
[33] Iourokina, I. V., and Lele, S. K., 2005, "Towards Large Eddy Simulation of Film-Cooling Flows on a Model Turbine Blade Leading Edge," AIAA Paper No. 2005-0670.
[34] Yang, Y.-T., and Wang, Y.-X., 2005, "Three-Dimensional Numerical Simulation of an Inclined Jet With Cross-Flow," Int. J. Heat Mass Transfer, **48**, pp. 4019–4027.
[35] Guo, X., Schröder, W., and Meinke, M., 2006, "Large-Eddy Simulations of Film Cooling Flows," Comput. Fluids, **35**(6), pp. 587–606.
[36] Li, Z., Murugappan, S., Gutmark, E., and Vallet, L., 2006, "Numerical Simulation and Experiments of Jets in Cross Flow," AIAA Paper No. 2006-307.
[37] Majander, P., and Siikonen, T., 2006, "Large-Eddy Simulation of a Round Jet in a Cross-Flow," Int. J. Heat Fluid Flow, **27**(3), pp. 402–415.
[38] Pathak, M., Dass, K. A., and Dewan, A., 2008, "An Investigation of Turbulent Rectangular Jet Discharged Into a Narrow Channel Weak Crossflow," J. Hydrodyn., **20**(2), pp. 154–163.
[39] Reddy, D. R., and Zaman, K. B. M. Q., 2006, "Computational Study of Effect of Tabs on a Jet in a Cross Flow," Comput. Fluids, **35**(7), pp. 712–723.
[40] Salewski, M., Stankovic, D., Fuchs, L., and Gutmark, E. J., 2006, "Coherent Structures in Circular and Non-Circular Jets in Crossflow," AIAA Paper No. 2006-907.
[41] Jouhaud, J. C., Gicquel, L. Y. M., Enaux, B., and Esteve, M.-J., 2007, "Large-Eddy-Simulation Modeling for Aerothermal Predictions Behind a Jet in Crossflow," AIAA J., **45**(10), pp. 2438–2447.
[42] Morris, R. M., Snyman, J., and Meyer, J., 2007, "Jets in Crossflow Mixing Analysis Using Computational Fluid Dynamics and Mathematical Optimization," J. Propul. Power, **23**(3), pp. 618–628.
[43] Rusch, D., Blum, L., Moser, A., and Roesgen, T., 2008, "Turbulence Model Validation for Fire Simulation by CFD and Experimental Investigation of a Hot Jet in Crossflow," Fire Saf. J., **43**(6), pp. 429–441.
[44] Ziefle, J., and Kleiser, L., 2009, "Large-Eddy Simulation of a Round Jet in Crossflow," AIAA J., **47**(5), pp. 1158–1172.
[45] Priere, C., Gicquel, L. Y. M., Kaufmann, P., Krebs, W., and Poinsot, T., 2004, "Large Eddy Simulation Predictions of Mixing Enhancement for Jets in Cross-Flows," J. Turbul., **5**(4), pp. 1–24.
[46] Sun, O. S., and Su, L. K., 2004, "Experimental Assessment of Scalar Mixing Models for Large-Eddy Simulation," AIAA Paper No. 2004-2550.
[47] Huang, Y., and Yang, V., 2009, "Dynamics and Stability of Lean-Premixed Swirl-Stabilized Combustion," Prog. Energy Combust. Sci., **35**(4), pp. 293–364.
[48] Swanson, R. C., and Turkel, E., 1992, "On Central-Difference and Upwind Schemes," J. Comput. Phys., **101**(2), pp. 292–306.
[49] Wang, S., and Yang, V., 2005, "Unsteady Flow Evolution in Swirl Injectors With Radial Entry—II: External Excitations," Phys. Fluids, **17**, p. 045107.
[50] Lu, X., Wang, S., Sung, H.-G., Hsieh, S.-Y., and Yang, V., 2005, "Large-Eddy Simulations of Turbulent Swirling Flows Injected Into a Dump Chamber," J. Fluid Mech., **527**, pp. 171–195.
[51] Zhang, L., 2011, "Flow Dynamics and Scalar Mixing of Transverse Jets Into Crossflows," Ph.D. thesis, The Pennsylvania State University, State College, PA.
[52] Eggels, J. G. M., Unger, F., Weiss, M. H., Westerweel, J., Adrian, R. J., Friedrich, R., and Nieuwstadt, F. T. M., 1994, "Fully Developed Turbulent Pipe Flow: A Comparsion Between Direct Numerical Simulation and Experiment," J. Fluid Mech., **268**, pp. 175–209.
[53] Lu, G., and Lele, S. K., 1993, "Inviscid Instability of a Skewed Compressible Mixing Layer," J. Fluid Mech., **249**, pp. 441–463.
[54] Denev, J. A., Fröhlich, J., and Bockhorn, H., 2009, "Large Eddy Simulation of a Swirling Transverse Jet Into a Crossflow With Investigation of Scalar Transport," Phys. Fluids, **21**(1), pp. 1–20.